JOURNAL OF PROPULSION AND POWER
Vol. 19, No. 3, May–June 2003

# Effect of Nozzle Cavity on Resonance in Large SRM: Numerical Simulations

J. Anthoine* and J.-M. Buchlin†
*von Kármán Institute for Fluid Dynamics, 1640 Rhode-St-Gènese, Belgium*
and
J.-F. Guéry‡
*SNPE, 91710 Vert-le-Petit, France*

**The nozzle design effect on sound production is investigated to improve the understanding of the aeroacoustic coupling that occurs in solid rocket motors with a submerged nozzle. Earlier analytical and experimental work demonstrated that flow–acoustic coupling is observed only for submerged nozzles for which the sound pressure level increases linearly with the nozzle cavity volume. Numerical simulations of the flow–acoustic coupling phenomena and in particular of the effect of the nozzle cavity volume on the pressure pulsations are performed using the code CPS. The numerical and experimental pressure spectra are compared. The frequencies are well simulated by the numerical code even if the pressure levels are overestimated. The nozzle design effect on sound production is also observed with a reduction of pressure level of 55% when the nozzle cavity is removed. Furthermore, the nozzle cavity modifies the flowfield around the nozzle head. With the cavity, the recirculation bubble is shorter, and the flow close to the nozzle head presents high amplitudes of radial mean velocity and fluctuation. That explains why the vortices break up when interacting with the nozzle head. With the cavity, the vortices shed by the inhibitor move along the border of the recirculation bubble and then pass in front of the cavity entrance, where they generate sound by interacting with the velocity fluctuations induced by the cavity volume. This results in a strong interaction between the vortices and the nozzle, which leads to large pressure oscillations.**

## Nomenclature

| | | |
|---|---|---|
| $a$ | = | sound speed |
| $D$ | = | internal diameter of the model |
| $d$ | = | internal diameter of the inhibitor |
| $f$ | = | frequency of the oscillation |
| $He$ | = | Helmholtz number |
| $j$ | = | excited acoustic mode number |
| $L$ | = | total length |
| $l$ | = | inhibitor–nozzle distance |
| $M_0$ | = | mean Mach number |
| $\mathcal{P}$ | = | average acoustic power |
| $p_s$ | = | mean static pressure |
| $p'$ | = | oscillatory pressure |
| $r$ | = | radial coordinate |
| $\boldsymbol{u}'$ | = | oscillatory velocity vector |
| $V_c$ | = | nozzle cavity volume |
| $\boldsymbol{v}$ | = | vortex transport velocity vector |
| $x$ | = | axial coordinate |
| $\gamma$ | = | ratio of specific heats |
| $\rho_0$ | = | mean density |
| $\boldsymbol{\omega}$ | = | vorticity vector |

## Introduction

THE present research is a numerical study of aeroacoustic phenomena occurring in large solid rocket motors (SRM) such as the Ariane 5 boosters. The emphasis is given to aeroacoustic instabilities that may lead to internal pressure and thrust oscillations that reduce the rocket motor performance. The study is carried out within the framework of a Centre National d'Etudes Spatiales (France) research program.

The Ariane 5 SRM has a segmented combustion chamber consisting of three propellant grains, separated by inhibitor rings ensuring thermal protection, and a submerged nozzle (Fig. 1). This accelerator, as other large SRM, presents large-amplitude low-frequency pulsations.[1–5] The amplitude of the pressure fluctuations may reach a few thousands of the static pressure in the combustion chamber [$p'/p_s \simeq \mathcal{O}(10^{-3})$]. These vibrations are damped out to the launcher and its payload by passive control systems, which can increase cost and reduce performance.

Solid rocket flows are complex. The propellant combustion generates a radial flow whose analytical solution has been obtained first by Taylor[6] in cylindrical geometries and constant mass flow rate. Then the flow develops longitudinally before reaching the exhaust nozzle. Three types of hydrodynamic instabilities appear to occur in solid rocket flows and are organized in coherent structures, called vortices. The first type of hydrodynamic instability, called angle vortex shedding (AVS), can occur at geometrical irregularities such as grooves in the grain. When developed at the inhibitor rings, the hydrodynamic instability is called obstacle vortex shedding (OVS). In the early studies of the pressure oscillations occurring in SRM, it was believed that the inhibitors were the only cause of the formation of vortices and of pulsations.[1,7] Dotson et al.[4] showed that pulsations could appear without the presence of inhibitors. It was demonstrated that the Taylor[6] flow is linearly unstable[8] and features another hydrodynamic instability leading to vortices called surface vortex shedding (SVS).[9–11]

The vortices generated by the hydrodynamic instabilities described (AVS, OVS, and SVS) are advected toward the submerged nozzle and interact with it. The sound produced by these interactions excites the acoustic properties of the combustion chamber. When the vortex shedding frequency synchronizes one of the first longitudinal acoustic modes of the motor chamber, resonant coupling may occur which leads to self-sustained oscillations. Then the vortices are generated at the frequency of that excited acoustic mode, closing the flow acoustic feedback loop.

Received 21 May 2002; revision received 13 January 2003; accepted for publication 13 January 2003. 

*Assistant Professor, Environmental and Applied Fluid Dynamics Department, Chaussée de Waterloo 72; anthoine@vki.ac.be. Member AIAA.

†Professor, Environmental and Applied Fluid Dynamics Department, Chaussée de Waterloo 72.

‡Head, Computational Fluid Dynamics Group, Centre de Recherches du Bouchet, BP 2. Member AIAA.

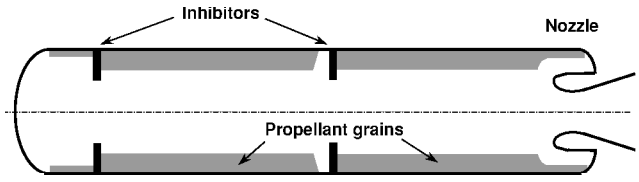


**Fig. 1 Internal geometry of Ariane 5 SRM.**

Stability assessment methods based on linear analytical theories initially predicted most of the large SRM to be stable.[12] Recently, Flandro and Majdalani[13] introduced a new term in the stability assessment methods to account for the presence of surface vortex shedding, which explained the instabilities in existing SRM.

Cold-flow experiments in a pipe with one or two diaphragms, in which only OVS occurs, were conducted to explain the flow acoustic coupling.[14–19] The influence of radial injected flow and SVS on the flow–acoustic coupling was then experimentally investigated.[7,11] Vortex-driven acoustically coupled oscillations were also observed on subscaled model rockets.[10,20,21] Finally, numerical simulations were used to highlight the three types of hydrodynamic instabilities and their coupling with the acoustics.[22–25]

These various studies point out that the potential source of the pressure pulsations is the sound production due to vortex–nozzle interactions.[14] The nozzle geometry is then expected to play an important role in the amplification of the sound pressure fluctuations.

The present research is aimed at investigating numerically the flow–acoustic coupling phenomena and, in particular, the effect of the nozzle cavity volume on the pressure pulsation levels. That effect was already observed in cold-flow experiments and explained by a simple analytical model.[14] Therefore, the numerical data will be compared to the existing analytical and experimental results. Our final aim is to understand the aeroacoustic phenomena that occur in segmented boosters such as Ariane 5.

## Earlier Analytical and Experimental Results

Flandro and Jacobs[26] linked the oscillations to the hydrodynamic instability of the sheared regions of the flow and to the coupled acoustical response of the motor. Because for the low frequencies investigated combustion is believed to take a minor part in the instability mechanism, most laboratory experiments were carried out with models operating with cold gases. As discussed earlier, the work of Vuillot,[22] Dotson et al.,[4] and Casalis et al.[9] has indicated that the presence of inhibitors is not necessary to drive the oscillations. In our experiments, however, we will not have a radial cold-gas injection, but rather an axial injection through the forward end of the model. In such a case, an inhibitor is placed to produce the necessary vortex shedding, and the confined space of the pipe acts as a resonator with its natural frequencies. Pressure oscillation reaches a large amplitude when the vortex shedding frequency is close to the frequency of one resonant acoustic mode of the system. The presence of an obstacle downstream of the shedding point of the vortices provides the necessary acoustical feedback when the vortices interact with it.[7] In our case, this second obstacle is the nozzle. We focus on the interaction of the vortices with the nozzle at the backward end of the model.

### Analytical Model

Vortex nozzle interaction is studied numerically later in this paper. We first present a simple analytical model.[14] A key to our nonlinear approach is to assume that the structure of the vortices reaching the nozzle is independent of the acoustical amplitude. The vortex formation is triggered by the acoustical flow, but the vortices concentrate the vorticity of the entire flow. The acoustical perturbations have only a minor effect on the amount of vorticity and the path of the vortex at the nozzle.[19]

When vortices approach the nozzle inlet, their transport velocity vector is significantly deviated from the acoustical streamlines (potential flow). According to Howe,[27] they produce sound when this occurs. Hence, we should translate the "impingement" of Flandro and Jacobs[26] as vortex–sound interaction localized at the nozzle inlet (see Ref. 28). We will now show, by means of an analytical model, that this interaction is stronger for a submerged nozzle because of the presence of a cavity around the nozzle head.

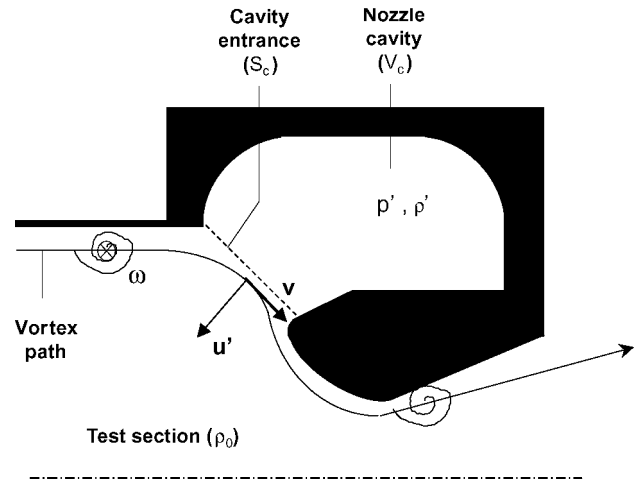


**Fig. 2 Theoretical modeling of the vortex–nozzle interaction.**

The model is based on the vortex–sound theory developed by Powell[29] and Howe.[30] The vortex–sound theory assumes some existing knowledge of the vortical distribution in the flow and deduces the aeroacoustical sound production from this knowledge.[28] At low Mach numbers as in this case, the vortex–sound theory yields the acoustic power given by

$$\mathcal{P} = -\rho_0 \left\langle \int_V (\boldsymbol{\omega} \times \boldsymbol{v}) \cdot \boldsymbol{u}' \, \mathrm{d}V \right\rangle \tag{1}$$

and represents the time average of the power transfer from the vorticity field to the acoustical field. $V$ is the source volume (where $\boldsymbol{\omega} \neq 0$) and the brackets indicate the averaging over one period of a steady oscillation.

As shown later in the experimental part, the nozzle cavity promotes higher resonance when the volume of the cavity is larger. The compressibility of the gas in the cavity volume induces an acoustic fluctuation $u'$ at the cavity inlet (Fig. 2). When the vortices travel in front of the cavity entrance, the acoustic velocity $\boldsymbol{u}'$ is almost normal to the vortex path $\boldsymbol{v}$. Therefore, our model should provide an upper bound for the pulsation amplitude, which after mathematical developments is given by

$$|p'|/p_s \sim [\pi\gamma/(\gamma - 1)]\, j\, M_0 (V_c/V_{\text{tot}}) \tag{2}$$

where

$$V_{\text{tot}} = (\pi D^2/4)L \tag{3}$$

A detailed description of the model and of its limitation has been presented by Anthoine et al.[14] When resonance occurs, the sound pressure level is a linear function of the Mach number, the excited mode number, and the nozzle cavity volume.

### Cold-Flow Experiments

The numerical data presented later will be compared to cold-flow experiments conducted by Anthoine et al.[14,19] The purpose of this section is to describe briefly the experimental setup and results that are used later to validate our numerical simulations.

The experimental facility is a 1/30th-scale modular axisymmetric cold-flow model of the Ariane 5 SRM, with a fully axial flow injected through the forward end. The model (Fig. 3) consists of a cylindrical test section, with an inhibitor of orifice diameter $d$ placed at a distance $l$ from a nozzle with sonic condition at the throat.[31] The internal diameter $D$ of the segments, equal to 0.076 m, is based on the 1/30th-scale similarity with the full-scale motor obtained by conserving the Mach number when 50% of the propellant is burnt. The

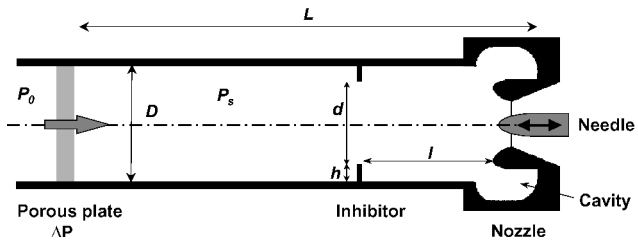


**Fig. 3 Axisymmetric setup, 1/30th scale.**

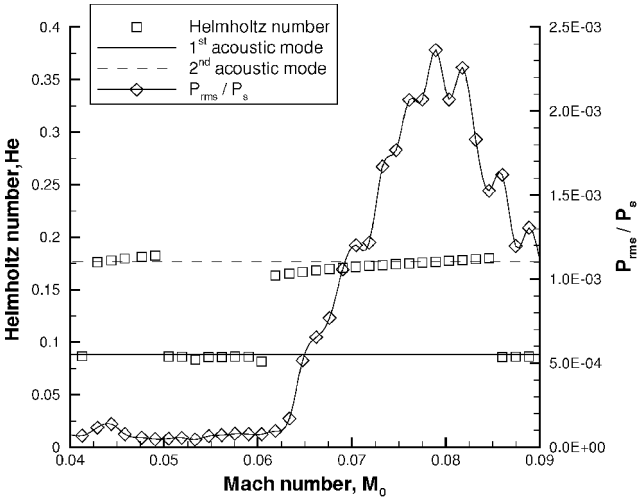


**Fig. 4 Evolution of the maximum of the pressure fluctuation, in terms of Helmholtz number and amplitude: $L = 393$ mm, $l = 71$ mm, and $d = 58$ mm, nozzle 1; $V_c = 2 \times 10^{-4}$ m$^3$.**

total length $L$ and the inhibitor parameters $d$ and $l$ can be modified. Compressed air is supplied through a porous plate at the forward end of the test section. That porous plate provides a high-pressure drop necessary to ensure an acoustic insulation of the test section from the air supply. Different nozzles can be tested to analyze the effect of the volume of the nozzle cavity on the pulsation levels.[32] Pressure oscillations are acquired by means of a piezoelectric pressure probe and are analyzed to determine the power spectrum with a frequency resolution of 1.8 Hz.

Pressure fluctuations are measured at the forward end (just downstream of the porous plate) for an inhibitor with orifice diameter of $d = 0.058$ m placed at a distance $l = 0.071$ m from the head of a nozzle of cavity volume $V_c$ ranging from 0 to $2 \times 10^{-4}$ m$^3$. The exact value of the length $L$ of the test section depends on the nozzle geometry and is approximately $L = 0.38$ m. The maximums of the pressure fluctuation amplitudes are plotted vs Mach number $M_0$ in Fig. 4. The evolution of the Helmholtz number ($He = fl/a$) corresponding to the maximum of the pressure fluctuations is also given in Fig. 4. In Fig. 4, the horizontal lines correspond to the longitudinal acoustic modes of the test section characterized by $He_{\mathrm{ac},j} = jl/(2L)$. Each time the excited frequency is close to an acoustic mode frequency, the pressure fluctuation level is large. The maximum is reached when it crosses the acoustic mode. Look at Fig. 4: The maximum of the sound pressure level is observed experimentally to excite the second longitudinal acoustic mode at a Mach number $M_0 = 0.08$. The order of magnitude of the pulsation levels corresponds to the data on pressure fluctuations in SRM reported in the literature.[1,3,4]

The flow–acoustic coupling identified in Fig. 4 relies on the interaction between the vortices and the nozzle. Therefore, the nozzle geometry is expected to play an important role in the amplification of the sound pressure fluctuations. Indeed, by changing the nozzle design, the downstream obstacle at which vortices generate the acoustic waves is modified. Anthoine et al.[14] showed that the evolution of the Helmholtz number is similar for all of the nozzles with a cavity. The maximum of sound pressure levels that corresponds to the maximum of coupling does excite the second longitudinal acoustic mode and does appear at a Mach number of 0.08 whatever the nozzle geometry. However, the amplitude of the maximum resonance depends on the nozzle design, as expected from the application of the vortex–sound theory discussed earlier. When the volume of the nozzle cavity decreases, the pressure fluctuation lessens. That effect is summarized in Fig. 5. Only the nozzles presenting a cavity and excitation on the second acoustic mode at $M_0 = 0.08$ are considered. The evolution of the maximum sound pressure level is approximately linear with the nozzle cavity volume. Such a finding is in agreement with relation (2). The amplitude predicted by our model is, however, too large by two orders of magnitude.

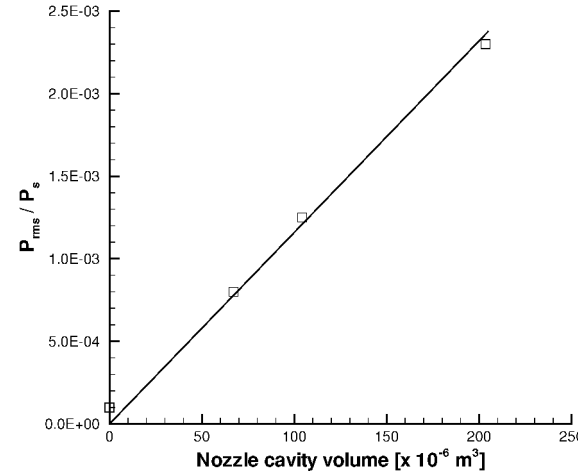


**Fig. 5 Evolution of the maximum sound pressure level vs the nozzle cavity volume for excitation on the second acoustic mode at $M_0 = 0.08$: $l = 71$ mm and $d = 58$ mm.**

## CPS Code

The acoustic investigation carried out experimentally proved the strong effect of the nozzle design on the sound pressure levels. The purpose of the following sections is to simulate the same operating conditions using the numerical code CPS. The CPS code is supported by the Centre National d'Etudes Spatiales and SNPE and is based on PATRIC code, which has been developed and upgraded for 15 years at SNPE,[24,33,34] and which is applied to CFD computations of unsteady flows in SRM. Today the code is used to solve the two-dimensional axisymmetrical, plane, and three-dimensional Navier–Stokes equations for laminar or turbulent flows with a cell-centered finite volume method. To simulate vortex shedding, two-equation turbulence models, such as the $(q, \omega)$ or $(k, \epsilon)$ models, are not efficient without specific treatments for coherent structures.[35] These improved models are currently under study in CPS, but are not used in the present paper. However, the time-dependent solution of the complete Navier–Stokes equations without a specific turbulence model allows direct simulation of all of the structures larger than the mesh cell size.[24] This approach corresponds to a very large-eddy simulation (VLES) without subgrid models. In this case, a grid dependency analysis has to be performed to investigate the convergence. The computations presented in this paper have been carried out applying such a VLES approach.

The code also includes the possibility for treating the chemical reactions of multispecies and the coupling between a gas phase and a condensed phase, inert or not. The code has moving mesh facilities. The behavior of the propellant goes from simple laws (regression rate) to several couplings (erosive burning, pressure response) as well as structure or regression rate coupling. All of the models are coupled to each other.

Two computations have been carried out to simulate the experimental test section (Fig. 3). Two nozzles, submerged and not are considered. For the two investigations, the two-dimensional axisymmetrical, unsteady Navier–Stokes equations are solved

under the assumption of a laminar flow, with inert gas at $\gamma$ constant. The second-order spatial discretization is applied, and the time integration uses the explicit second-order Runge–Kutta scheme.

## Numerical Simulation with Submerged Nozzle

The aim of the simulation is to obtain data, such as flowfield results, that are not available from the experiments. Because the validation of the code is first needed, the experimental test section is simulated. However, it has been decided not to consider the presence of the needle in the nozzle. Therefore, the computations are performed for the nominal experimental conditions corresponding to a Mach number $M_0 = 0.09$. Even if that Mach number does not correspond to the maximum of pressure oscillations observed experimentally at $M_0 = 0.08$, the comparison between the experimental and numerical data will be made at $M_0 = 0.09$.

The first case to be simulated with the CPS code is the axial injected flow configuration with the submerged nozzle, as shown in Fig. 6. The nozzle has the same geometry as experimental nozzle 1 with a throat diameter of 0.03 m (Fig. 3). The cylindrical numerical domain has an inner diameter $D$ of 0.076 m. The total length $L$ is equal to 0.393 m and an inhibitor of 0.058 m inner diameter $d$ is placed at $l = 0.071$ m from the nozzle head.

### Mesh and Boundary Conditions

The numerical domain consists of quadrilateral control cells, with refinements between the inhibitor and the nozzle head and in the nozzle cavity and throat (Fig. 7). The grid is composed of 13591 elements. A grid-dependency analysis proved that a higher refinement is not necessary and that the VLES approach is correct.[36]

The cold air is injected axially by imposing a constant mass flow rate through the forward end of the numerical domain considered as a hard-wall from the acoustics (Fig. 6). To allow comparison to the experimental data, the mass flow rate per surface unit is equal to 66.3 kg/s/m$^2$. The boundary condition at the exit of the nozzle corresponds to a pressure of 10 kPa. The bottom part of the numerical domain is the axis of symmetry. All of the other boundaries are characterized by a no-slip condition with the walls at 285 K.

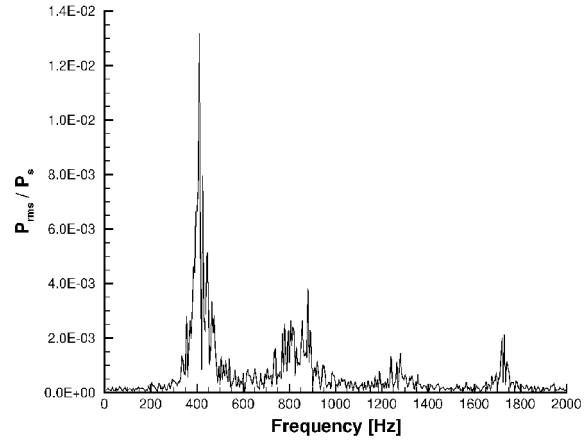


**a) CPS simulation**

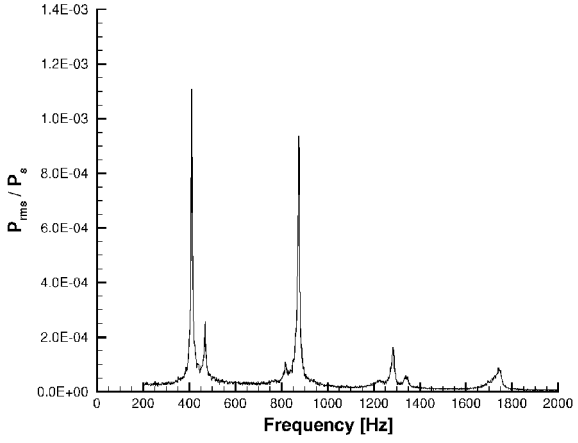


**b) Experiment**

**Fig. 8 Comparison of pressure spectrum for the simulation with a submerged nozzle. The numerical and experimental signals are both obtained at $x = 0.0115$ m and $r = 0.038$ m (point 1).**

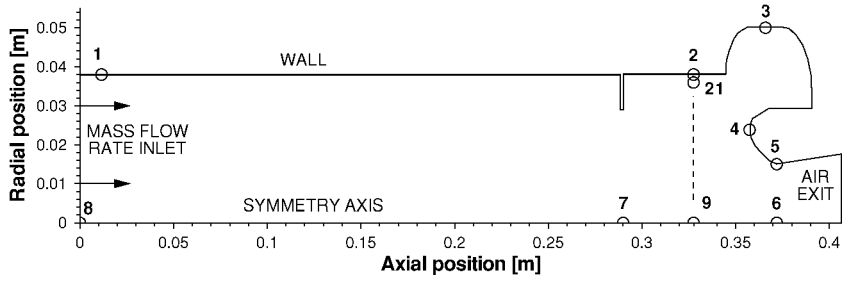


**Fig. 6 Geometry of the numerical domain with submerged nozzle, boundary conditions, and position of the virtual sensors.**

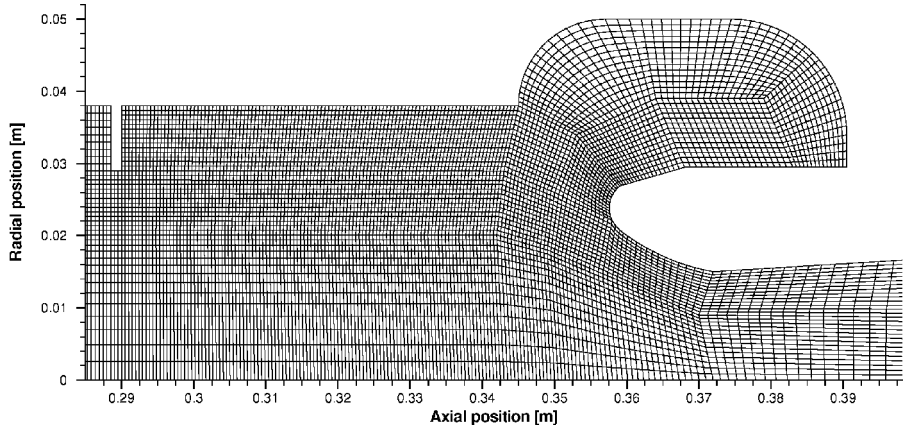


**Fig. 7 Mesh downstream of the inhibitor.**

**Unsteady Simulation**

The simulation starts by carrying out about one 100,000 iterations, to obtain an unsteady pressure signal with a good convergence of the solution. Then, the unsteady simulation is restarted for a physical time of 0.2 s for computation of the sound pressure level. The variations of the pressure, density, and velocity components at 21 virtual sensors, indicated in Fig. 6, are saved. Some of the sensors correspond to the experimental pressure fluctuation probes. The unsteady signals are analyzed to determine the response spectrum by computing the Fourier transform. The computation time of 0.2 s provides a frequency resolution of 5 Hz.

Figure 8a shows the sound pressure spectrum for the sensor 1. (The spectra for the other sensors are given in Ref. 36.) The pressure spectrum at the forward end contains four peaks located at 410, 840, 1270, and 1725 Hz, respectively. They correspond to the excitation of the first four longitudinal acoustic modes. The first one is the more energetic one with a maximum sound pressure level of 2350 Pa, corresponding to $p'/p_s = 1.3 \times 10^{-2}$.

The numerical sensor 1 is placed at the same location as one of the experimental probes. Therefore, the numerical and experimental sound pressure spectra can be compared in Fig. 8. The simulation predicts correctly the pressure peaks in the frequency domain. However, the experimental levels are one order of magnitude below those obtained from the numerical computations. Even by taking into account the acoustic losses induced by the porous head end, the numerical levels are still too high.[36] The overestimation could be explained by turbulent dissipation or two-dimensional to three-dimensional transition. Because the computations are performed applying a two-dimensional VLES approach, the three-dimensional turbulent dissipation is not simulated. In axial flow injection, the vortex ring shed by the inhibitor becomes rapidly unstable leading to a three-dimensional mode behavior. That transition is not simulated numerically in the present two-dimensional axisymmetrical computations. However, two-dimensional to three-dimensional transition has been observed from three-dimensional computations in presence of radial combustion.[24] Because the transition to a three-dimensional mode destroys the symmetry of the coherent structures, their interaction with the nozzle generates weaker pressure fluctuations. That could explain the difference between the experimental and numerical levels. Globally, the frequencies are well simulated by the numerical code even if the pressure levels are overestimated.

A sequence of vorticity fields is provided in Fig. 9. Each vortex shed by the inhibitor impinges on the nozzle head and

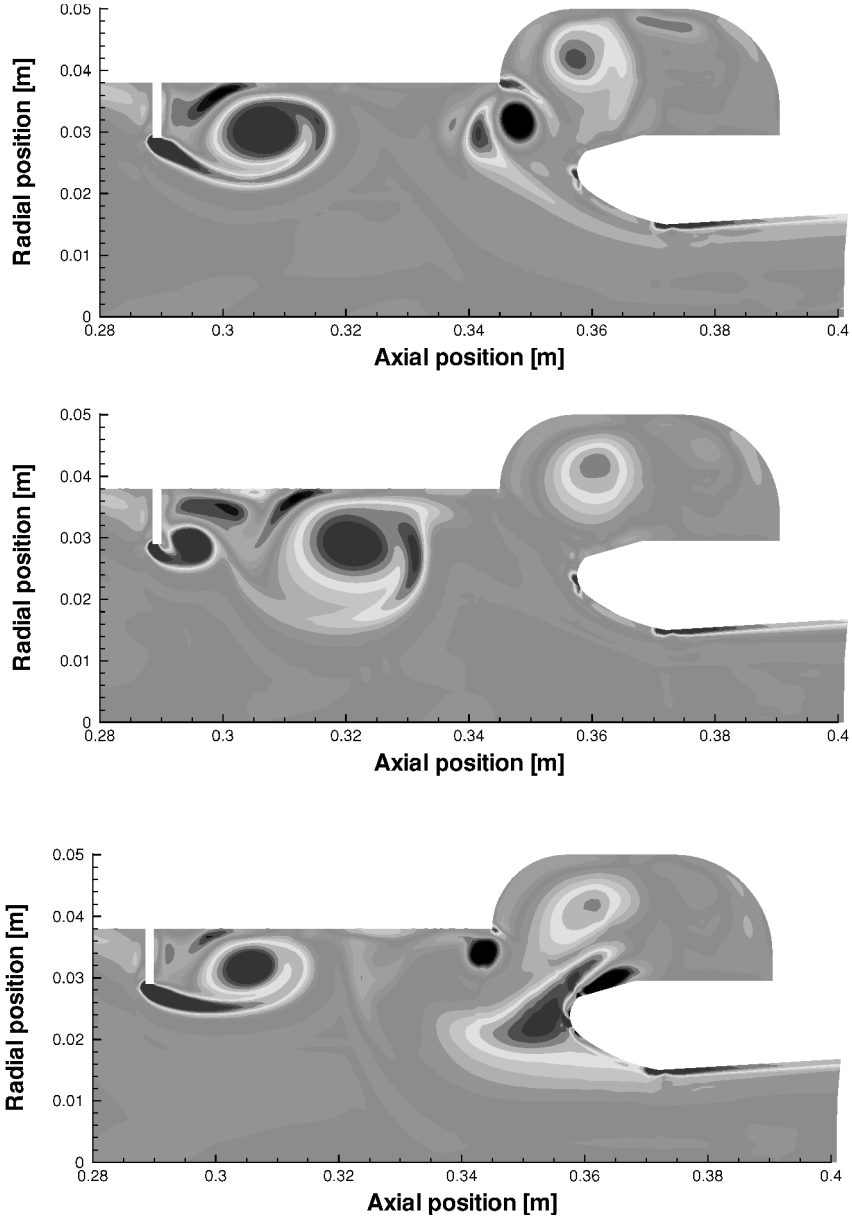


**Fig. 9 Sequence of vorticity fields; $\Delta t$ between two images = $9 \times 10^{-4}$ s.**

breaks up. A part of it is kept prisoner in the nozzle cavity while the rest is escaping through the nozzle throat. Pairing may also be observed.

**Mean Flow**

The mean values of the magnitude and fluctuation of the velocity are obtained by averaging the unsteady simulation over five periods of vortex shedding. The streamlines are provided in Fig. 10a. The recirculation bubble behind the inhibitor develops over an axial distance of $x/h = 6.2$, where $h$ is the inhibitor height. Anthoine et al.[37] have carried out an experimental investigation with an inhibitor–nozzle distance, such as $l/h = 27$, and have shown that the length of the recirculation bubble behind the inhibitor is approximately equal to $12h$. For the shorter inhibitor–nozzle distance used in this numerical simulation ($l/h = 8$), the recirculation bubble is, of course, limited to $8h$. It was expected that the recirculation would develop over the area between the inhibitor and the nozzle and that the attachment point be located on the nozzle head. The streamlines of Fig. 10a prove that the recirculation bubble is shorter than those expected. Three other bubbles appear in the nozzle cavity. The Mach number magnitude of the first recirculation bubble in the nozzle cavity is as strong as that found in the recirculation behind the inhibitor. Those high Mach number $M_0$ values in the nozzle cavity come from the part of vorticity entering the cavity when a vortex breaks up on the nozzle head. Figure 10b shows the velocity vector field.

The flow close to the nozzle head ($x = 0.3575$ m) exhibits high amplitudes of the radial mean velocity (Fig. 11). The negative values are induced by the nozzle convergence, whereas the positive ones prove that a part of the flow enters into the nozzle cavity. At the limit, on the nozzle head, the flow splits in two streams. One goes through the throat, the other gets into the cavity. That observation should be linked to the fact that the recirculation bubble attached to the inhibitor is limited to an axial distance of $x/h = 6.2$. Both observations explain why the vortices break up when interacting with the nozzle head, generating strong pressure fluctuations. A part of the vorticity is staying in the cavity, while the rest is exhausting through the throat.

Figure 12 provides the contour of velocity fluctuations for both components. The important axial velocity fluctuations close to the wall are induced by the recirculation bubble. They also present high values on all of the inhibitor–nozzle distances, whatever the radius, due to the flow acceleration induced successively by the inhibitor and the nozzle convergence. The radial velocity fluctuations are higher in the shear layer generated by the inhibitor and exhibit the effect of the vortices. Therefore, it is normal that their largest amplitude appears close to the nozzle head, where the vortex breakup occurs.

Figure 13 provides a comparison of the computed streamlines with those obtained experimentally using a particle image velocimetry (PIV)[19] technique. The experimental flowfield analyzed is of limited area because of the PIV window used. The two flowfields

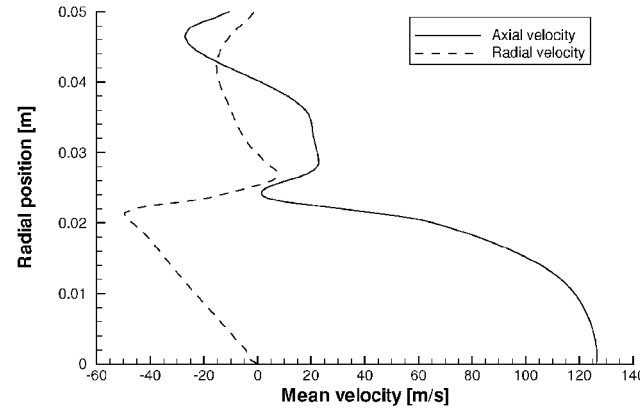


**Fig. 11 Axial and radial mean velocity profiles at $x = 0.3575$ m.**

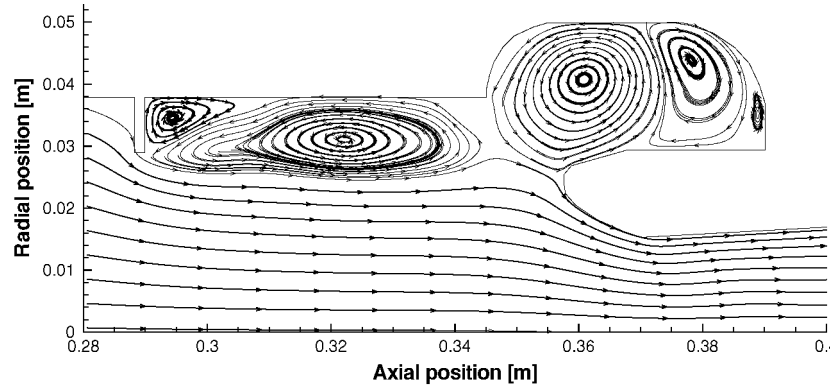


**a) Streamlines**

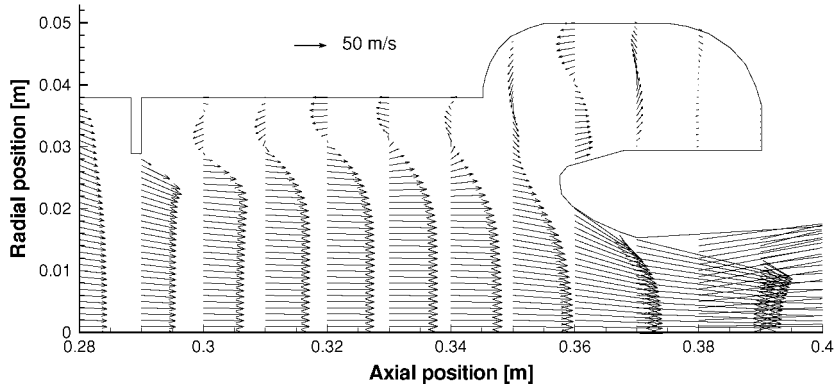


**b) Velocity vectors field**

**Fig. 10 Mean flowfield.**

are similar. The center of the recirculation bubble $(x_c, r_c)$ attached to the inhibitor is well reproduced by CPS, as shown in Table 1. To be more quantitative, profiles of mean velocity and of velocity fluctuation are compared in Fig. 14. The axial and radial mean velocity profiles are close, even if some deviations are observed at the limits of the recirculation bubble, where the velocity gradients are important. Although particular care was devoted to the application of the PIV technique, the image acquisition in an axisymmetrical model is delicate to implement, specially close to the wall. The shapes of the profiles of velocity fluctuation, in particular the position of their maximum values, are well reproduced by CPS, although the fluctuation amplitudes are always overestimated by the code. The overestimation could be explained, in part, by the turbulence dissipation and the difference in the acoustic resonance levels. Indeed, the velocity fluctuation is due to the vortices and jet acceleration, but also acoustic resonance. The PIV measurement is carried out in an experimental model that produces acoustic pressure fluctuation of 120 Pa, corresponding to acoustic velocity fluctuation of 0.3 m/s. The CPS computation yields pressure fluctuation of 2350 Pa, which leads to acoustic velocity fluctuation of 3.2 m/s. The difference of 3 m/s between the computational and experimental acoustic velocity fluctuations explains one-third of the deviation observed in the axial velocity fluctuation in Fig. 14b.

**Fourier Coefficient Analysis**

It is now interesting to identify which part of the physical domain presents a high response either to the first acoustic mode frequency or to the second one corresponding to the vortex shedding frequency. The analysis of the frequency response is based on the computation of the modulus and argument of

**Table 1 Position of the center of the recirculation bubble from CPS and PIV[a]**

| Coordinate, mm | CPS | PIV |
|---|---|---|
| $x_c$ | 32.0 | 35.5 |
| $r_c$ | 31.1 | 30.5 |

[a]Origin is on the axis at the inhibitor section.

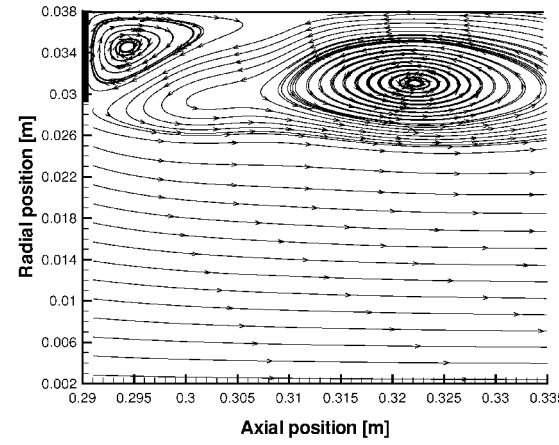


**a) CPS simulation**

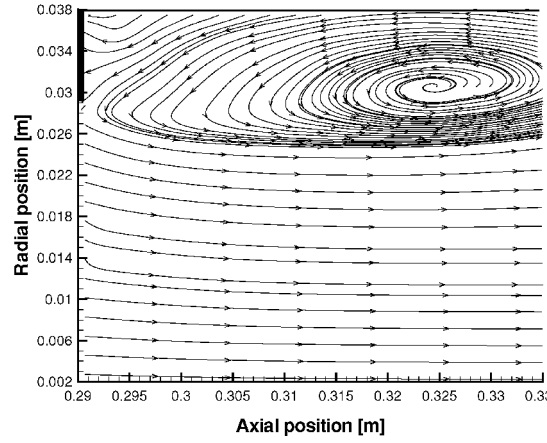


**b) PIV experiment**

**Fig. 13 Comparison of streamlines between numerical simulation and cold-flow experiment.**

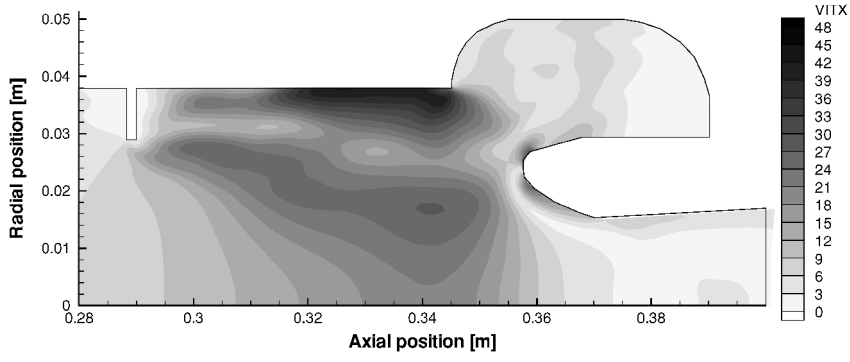


**a) Axial velocity fluctuations**

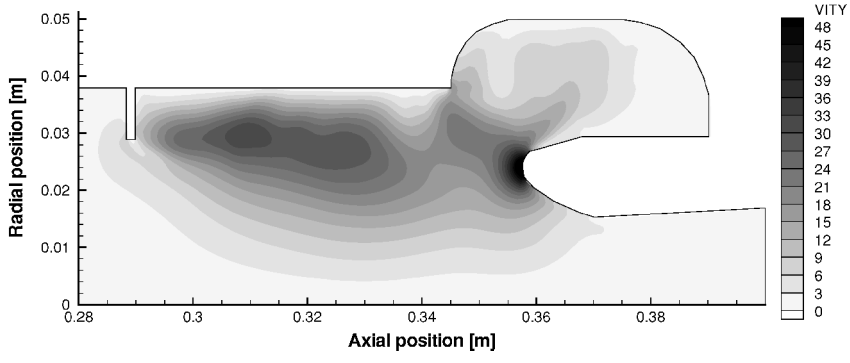


**b) Radial velocity fluctuations**

**Fig. 12 Contours of velocity fluctuations.**

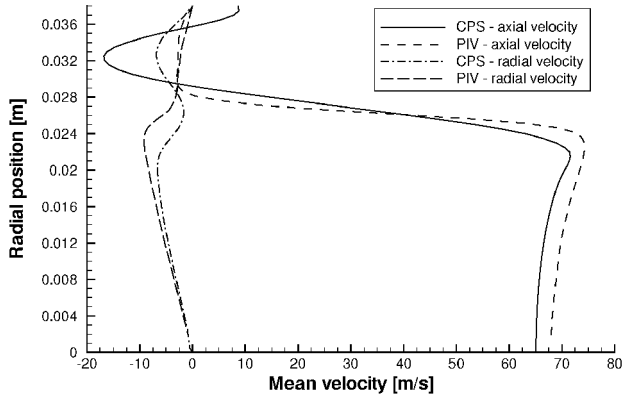


a) Mean velocity profiles

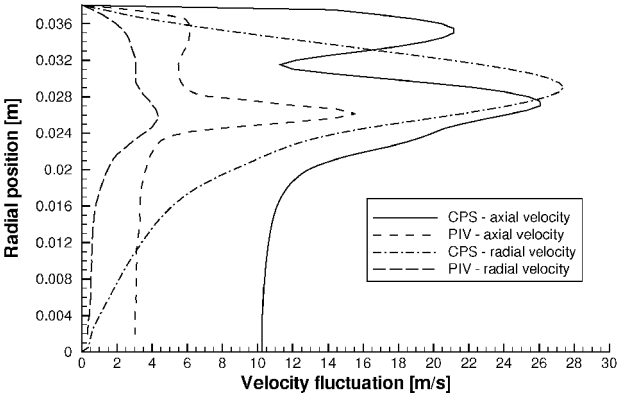


b) Velocity fluctuation profiles

**Fig. 14 Comparison of velocity profiles between numerical simulations and cold-flow experiments at $x = 0.3$ m.**

the complex Fourier coefficient $C$ for the pressure and velocity components:

$$C = \frac{2}{nT}\int_0^{nT} \phi e^{-i\omega t}\,\mathrm{d}t \tag{4}$$

where $n$ is the integer number of elapsed periods, $T$ is the period associated to the selected frequency $f$, $\omega = 2\pi f$ is the angular frequency, $\phi$ is the physical variable (pressure or velocity components), and $t$ is the time.

Profiles of the Fourier coefficient modulus are given in Fig. 15 for the pressure and velocity components. These profiles are plotted along a line passing through the inhibitor edge (at $r = 0.029$ m) and parallel to the symmetry axis. One can observe the nodes and antinodes of pressure and velocity induced by the acoustics upstream the inhibitor. The nodes of pressure coincide with the antinodes of velocity, as expected. The profiles corresponding to the second acoustic mode ($f_{2L} = 840$ Hz) reveal a number of half-periods equal to two times those of the first acoustic mode ($f_{1L} = 410$ Hz). Moreover, the amplitude of the pressure and axial velocity moduli is higher for $f_{1L}$ than for $f_{2L}$.

Because the radial velocity modulus is almost nil upstream the inhibitor, the acoustic waves are plane in that part of the domain. The deviation of the acoustic waves induced by the inhibitor appears through jumps in the modulus. Downstream of the inhibitor ($x = 0.29$ m), the pressure and velocity moduli show maxima whose positions do not vary with the frequency, but their amplitudes are different. Fourier analyses prove that, upstream of the inhibitor, mean flow disturbances are purely acoustic, whereas downstream, both acoustics and hydrodynamics (vortex shedding) are present.

Figure 15a also shows a comparison of the numerical and experimental profiles of the Fourier coefficient modulus for the pressure. The experimental pressure modulus is scaled up to the numerical one based on their amplitudes at $x = 0$ m because the simulation

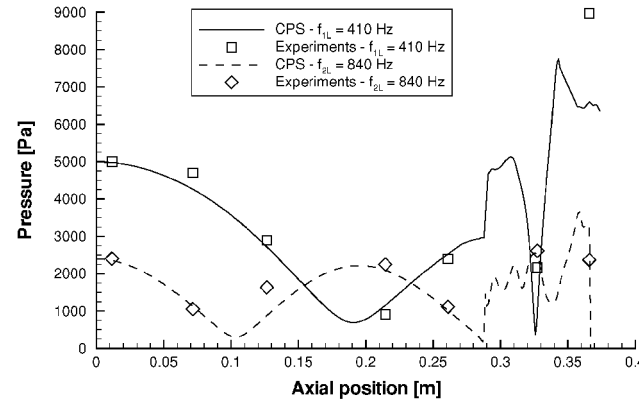


a) Relative pressure

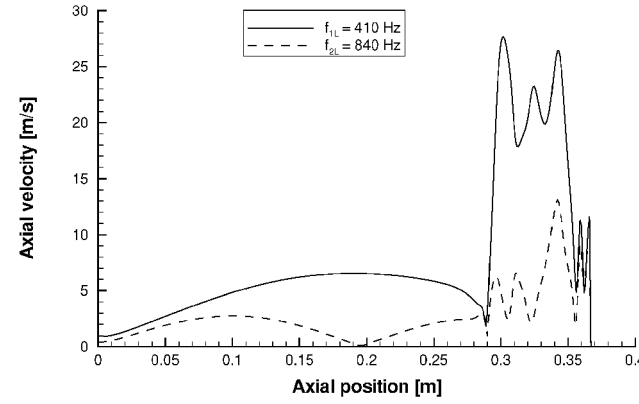


b) Axial velocity

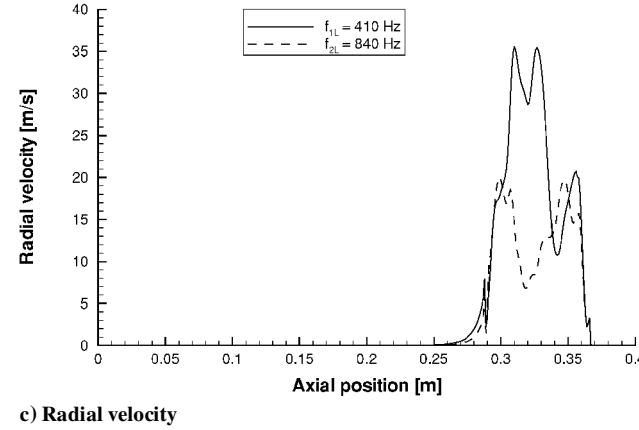


c) Radial velocity

**Fig. 15 Profiles of the Fourier coefficient modulus for the two first acoustic modes.**

and the experiment do not lead to levels in the same order of magnitude, as explained before. The measured data are obtained from an experiment involving seven piezelectric probes. The computed and experimental variations of the Fourier coefficient of the pressure calculated at the first and second acoustic modes are in good agreement.

## Influence of Nozzle Geometry

The next case simulated with the CPS code is the axial injected flow configuration with a convergent–divergent section nozzle without a cavity. The objective is to check if the strong effect of the cavity volume on the amplification of the sound pressure level can be simulated numerically. The geometrical parameters and the boundary conditions are identical to those of the simulation with the submerged nozzle. The mesh is generated similarly and is composed of 23,863 elements.

**Unsteady Simulation**

The unsteady computation is performed for a physical time of 0.2 s, after getting a converged unsteady signal. Figure 16 provides the pressure spectrum at point 1 for the simulation without a cavity at the nozzle, which can be compared to Fig. 8a. Without a cavity, only two peaks appear in the pressure spectrum at 430 and 930 Hz. Removing the cavity reduces the total length $L$ of the numerical domain from 0.393 to 0.36 m. Therefore, the frequencies $f_{\mathrm{ac},i}$ of the longitudinal acoustic modes, given by $f_{\mathrm{ac},i} = ia/(2L)$, are increased compared to the simulation with a submerged nozzle. Moreover, instead of getting an unique peak around the first acoustic mode, two distinct peaks at 405 and 455 Hz appear, as shown in Fig. 16. The second peak could be the hydrodynamic mode.

The most energetic mode is at 455 Hz with a maximum sound pressure level of 1050 Pa, corresponding to $p'/p_s = 5.9 \times 10^{-3}$. Such a pressure level is 55% smaller than those of the submerged nozzle. Therefore, in agreement with the the analytical prediction and the experimental observations (Fig. 5), CPS predictions confirm the strong effect of the nozzle design on the flow–acoustic coupling and on the amplification of the pressure fluctuations. Although the numerical reduction of 55% is not as important as the experimental decrease of 90% (at $M_0 = 0.09$), the effect is also observed numerically.

**Mean Flow**

The averaged computation is performed over five periods of the vortex shedding at 930 Hz. The streamlines are provided in Fig. 17. Figure 17 can be compared to Fig. 10a of the submerged nozzle. For the nozzle without a cavity, the recirculation bubble behind the inhibitor extends over the whole space between the obstacle and the nozzle because $x/h = 8$ is smaller than 12 and reattaches on the nozzle head.[37]

Velocity profiles are plotted in Fig. 18 for both velocity components and for the two nozzles with and without a cavity. Close to the inhibitor, the velocity profiles are similar for both nozzle geometries. When the nozzle head is approached, deviations are observed for radius greater than 0.024 m, especially for the radial mean velocity and fluctuation.

Because the two nozzle geometries lead to different spreadings of the recirculation bubble behind the inhibitor, the flow around the nozzle head and, then, the vortex–nozzle interaction are completely different. The mean vortex paths for the two nozzle geometries are illustrated in Fig. 19. When it is known that the vortices are shed from the inhibitor edge, the mean vortex path corresponds to the mean flow streamline starting from the inhibitor edge. Of course, the real vortices are not following this path, but their averaged paths can

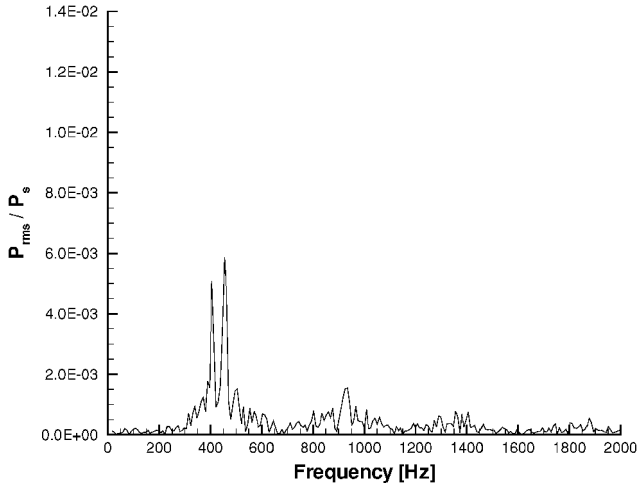


**Fig. 16 Pressure spectrum for the simulation without cavity at the nozzle; numerical signal is obtained at $x = 0.0115$ m and $r = 0.038$ m (point 1).**

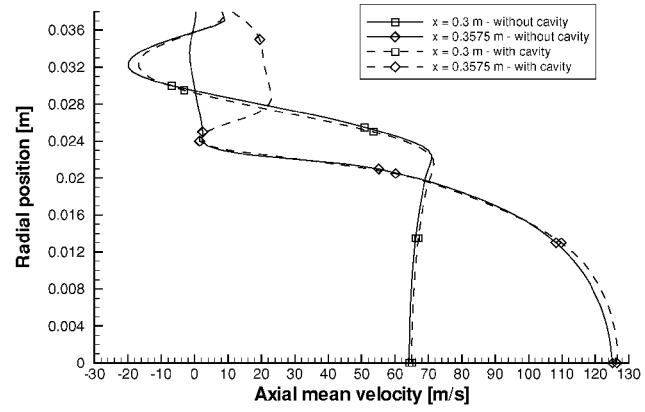


**a) Axial velocity**

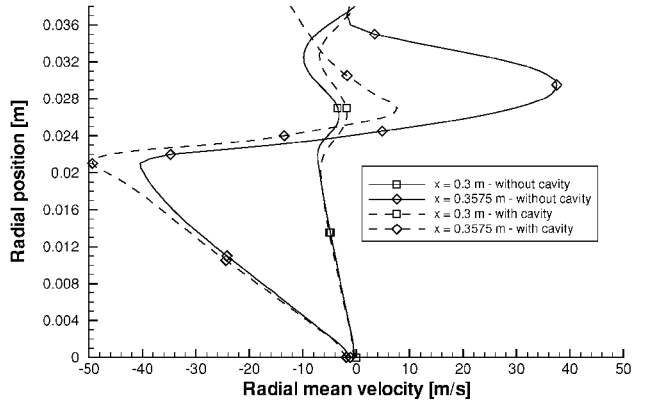


**b) Radial velocity**

**Fig. 18 Mean velocity profiles.**

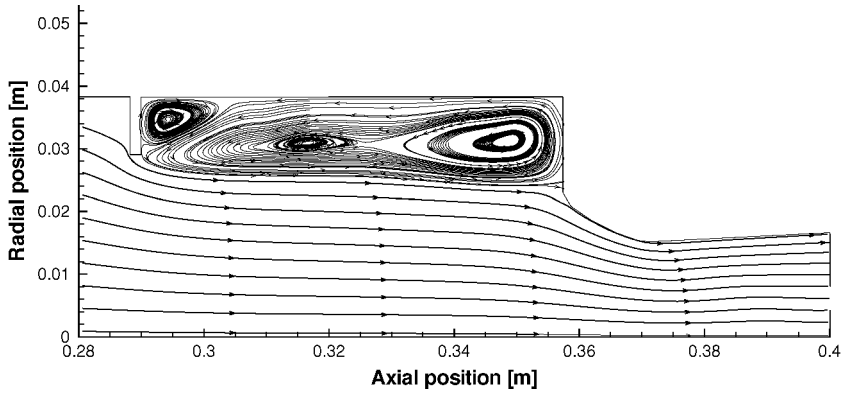


**Fig. 17 Mean flowfield.**

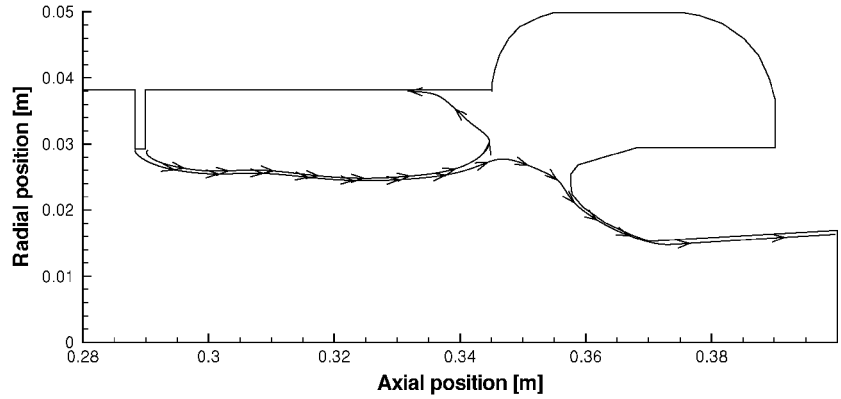


**a) Submerged nozzle**

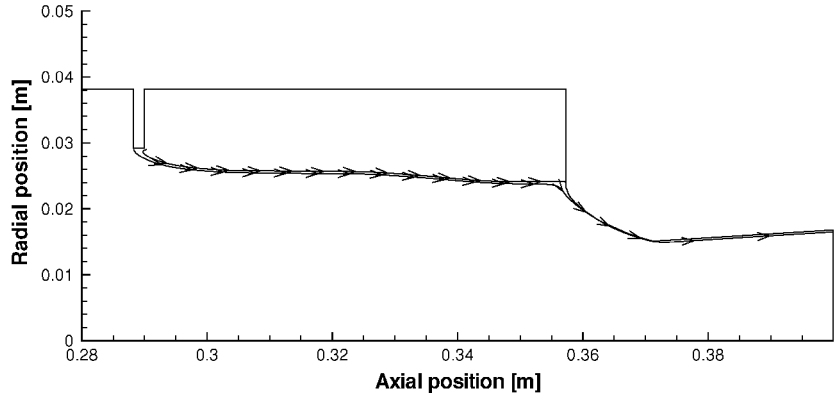


**b) Nozzle without cavity**

**Fig. 19 Mean vortex path for the nozzles with and without cavity.**

be approximated by this mean flow streamline. For the submerged nozzle, the vortices shed by the inhibitor move along the border of the recirculation bubble and then toward the cylindrical wall because of the positive radial velocities developing between the end of the bubble and the nozzle head. Then, the vortices pass in front of the cavity entrance, where they generate sound by interacting with the velocity fluctuations induced by the cavity volume. This results in a strong interaction between the vortices and the nozzle. When the cavity is removed, the vortices follow the border of the recirculation bubble that ends at the nozzle head and then escape directly through the nozzle without interacting with it. That explains the weaker pressure fluctuations measured without a nozzle cavity.

## Conclusions

The nozzle design effect on sound production was investigated to improve understanding of aeroacoustic coupling in SRM.

Earlier analytical and experimental studies have demonstrated that, in the case of a purely axial injected flow, flow–acoustic coupling is observed only for submerged nozzles. The maximum resonance amplitude is highly dependent on the nozzle design. The sound pressure level increases quite linearly with the nozzle cavity volume.

Numerical simulations of the flow–acoustic coupling phenomena and, in particular, of the effect of the nozzle cavity volume on the pressure pulsations have been performed using the code CPS. The numerical pressure spectra were compared to the acoustic pressure measurements performed in an axisymmetric cold-flow model of the Ariane 5 SRM. The frequencies are well simulated by the numerical code, even if the pressure levels are overestimated. The evolutions of the computed and experimental Fourier coefficients of the pressure are in good agreement. Without the cavity, the pressure level is 55% smaller than those of the submerged nozzle. Moreover, instead of getting an unique peak around the first acoustic mode, two distinct peaks are observed in the pressure spectrum. Although the numerical reduction of 55% of the pressure level is not as important as the experimental decrease of 90%, the nozzle design effect on sound production is also observed numerically.

Furthermore, the nozzle cavity resonance modifies the mean flowfield around the nozzle head. With the cavity, the recirculation bubble attached to the inhibitor is limited to an axial distance of $x/h = 6.2$, where $h$ is the inhibitor height, compared to $x/h = 8$ for the nozzle without a cavity. The reattachement point of the recirculation bubble is not located on the nozzle head. The flow close to the nozzle head also presents high amplitudes of radial mean velocity and fluctuation. At the limit, on the nozzle head, the flow splits in two streams. One goes through the throat, the other gets into the cavity. These observations explain why the vortices break up when interacting with the nozzle head. A part of the vorticity is staying in the cavity, while the rest is exhausting through the throat. With the cavity, the vortices shed by the inhibitor move along the border of the recirculation bubble and then pass in front of the cavity entrance where they generate sound by interacting with the velocity fluctuations induced by the cavity volume. This results in a strong interaction between the vortices and the nozzle, which leads to large-pressure oscillations.

## Acknowledgments

This study has been supported by ESA and the Centre National d'Etudes Spatiales (CNES). It is a part of the Aerodynamics of Segmented Solid Motors research program coordinated by CNES and ONERA. The numerical code CPS has been developed by SNPE and Bertin Technologies, under CNES and SNPE support.

## References

[1]Brown, R. S., Dunlap, R., Young, S. W., and Waugh, R. C., "Vortex Shedding as a Source of Acoustic Energy in Segmented Solid Rockets," *Journal of Spacecraft*, Vol. 18, No. 4, 1981, pp. 312–319.

[2]Blomshield, F. S., and Mathes, H. B., "Pressure Oscillations in Post-Challenger Space Shuttle Redesigned Solid Rocket Motors," *Journal of Propulsion and Power*, Vol. 9, No. 2, 1993, pp. 217–221.

[3]Scippa, S., Pascal, P., and Zanier, F., "Ariane–5 MPS: Chamber Pressure Oscillations Full Scale Firings Results Analysis and Further Studies," AIAA Paper 94-3068, June 1994.

[4]Dotson, K. W., Koshigoe, S., and Pace, K. K., "Vortex Shedding in a Large Solid Rocket Motor Without Inhibitors at the Segmented Interfaces," *Journal of Propulsion and Power*, Vol. 13, No. 2, 1997, pp. 197–206.

[5]Sukhinin, S. V., and Akhadeev, V. F., "Self-Oscillations in the Gas Cavity of a Solid Rocket Motor," *Combustion, Explosion and Shock Waves*, Vol. 37, No. 1, 2001, pp. 36–45.

[6]Taylor, G. I., "Fluid Flow in Regions Bounded by Porous Surfaces," *Proceedings of the Royal Society of London, Series A: Mathematical and Physical Sciences*, Vol. 234, No. 1199, 1956, pp. 456–475.

[7]Flatau, A., and VanMoorhem, W., "Prediction of Vortex Shedding Responses in Segmented Solid Rocket Motors," *Journal of Propulsion and Power*, Vol. 19, No. 2, 2003, pp. 287–297.

[8]Varapaev, V. N., and Yagodkin, V. I., "Flow Stability in a Channel with Porous Walls," *Fluid Dynamics (Izvestiya Akademii Nauk SSSR, Meckanika Zhidkosti i Gaza)*, Vol. 4, No. 5, 1969, pp. 91–95.

[9]Casalis, G., Avalon, G., and Pineau, J.-P., "Spatial Instability of Planar Channel Flow with Fluid Injection Through Porous Walls," *Physics of Fluids*, Vol. 10, No. 10, 1998, pp. 2558–2568.

[10]Prévost, M., Vuillot, F., and Traineau, J. C., "Vortex Shedding Driven Oscillations in a Subscale Motor for the Ariane 5 MPS Solid Rocket Motors," AIAA Paper 96-3247, July 1996.

[11]Yildiz, D., Anthoine, J., and Buchlin, J.-M., "Influence of Radial Injected Flow on the Aeroacoustic Coupling in Solid Propellant Boosters," AIAA Paper 2001-2101, May 2001.

[12]Lovine, R. L., and Waugh, R. C., "Standard Stability Prediction Method for Solid Rocket Motors," CPIA Publ. 273, Chemical Propulsion Information Agency, Laurel, MD, 1975.

[13]Flandro, G. A., and Majdalani, J., "Aeroacoustic Instability in Rockets," AIAA Paper 2001-3868, July 2001 (submitted for publication).

[14]Anthoine, J., Buchlin, J.-M., and Hirschberg, A., "Effect of Nozzle Cavity on Resonance in Large SRM: Theoretical Modeling," *Journal of Propulsion and Power*, Vol. 18, No. 2, 2002, pp. 304–311.

[15]Culick, F. E. C., and Magiawala, K., "Excitation of Acoustic Modes in a Chamber by Vortex Shedding," *Journal of Sound and Vibrations*, Vol. 64, No. 3, 1979, pp. 455–457.

[16]Dunlap, R., and Brown, R. S., "Exploratory Experiments on Acoustic Oscillation Driven by Periodic Vortex Shedding," *AIAA Journal*, Vol. 19, No. 3, 1981, pp. 408, 409.

[17]Hourigan, K., Welsh, M. C., Thompson, M. C., and Stokes, A. N., "Aerodynamic Sources of Acoustic Resonance in a Duct with Baffles," *Journal of Fluids and Structures*, Vol. 4, No. 4, 1990, pp. 345–370.

[18]Mettenleiter, M., Haile, E., and Candel, S., "Adaptive Control of Aeroacoustic Instabilities," *Journal of Sound and Vibration*, Vol. 230, No. 4, 2000, pp. 761–789.

[19]Anthoine, J., Mettenleiter, M., Repellin, O., Buchlin, J.-M., and Candel, S., "Influence of Adaptive Control on Vortex Driven Instabilities in a Scaled Model of Solid Propellant Motors," *Journal of Sound and Vibration* (to be published).

[20]Vuillot, F., Traineau, J. C., Prévost, M., and Lupoglazoff, N., "Experimental Validation of Stability Assessment Methods for Segmented Solid Propellant Motors," AIAA Paper 93-1883, June 1993.

[21]Traineau, J. C., Prévost, M., Vuillot, F., Le Breton, P., Cuny, J., Preioni, N., and Bec, R., "A Subscale Test Program to Assess the Vortex Shedding Driven Instabilities in Segmented Solid Rocket Motors," AIAA Paper 97-3247, July 1997.

[22]Vuillot, F., "Votex-Shedding Phenomena in Solid Rocket Motors," *Journal of Propulsion and Power*, Vol. 11, No. 4, 1995, pp. 626–639.

[23]Kourta, A., "Shear Layer Instability and Acoustic Interaction in Solid Propellant Rocket Motors," *International Journal for Numerical Methods in Fluids*, Vol. 25, No. 8, 1997, pp. 973–981.

[24]Mombelli, C., Guichard, A., Godfroy, F., and Guéry, J.-F., "Parallel Computation of Vortex Shedding in Solid Rocket Motors," AIAA Paper 99-2510, July 1999.

[25]Hulshoff, S. J., Hirschberg, A., and Hofmans, G. C. J., "Sound Production of Vortex Nozzle Interaction," *Journal of Fluid Mechanics*, Vol. 439, 2001, pp. 335–352.

[26]Flandro, G. A., and Jacobs, H. R., "Vortex Generated Sound in Cavities," AIAA Paper 73-1014, Oct. 1973.

[27]Howe, M. S., "The Dissipation of Sound at an Edge," *Journal of Sound and Vibration*, Vol. 70, No. 3, 1980, pp. 407–411.

[28]Hirschberg, A., Hulshoff, S., van Hassel, R. R., and Anthoine, J., "Vortex–Acoustic Interaction in Internal Flows: the Whistler-Nozzle, Human Whistling and the Solid-Propellant Rocket Motor," *Proceedings of the 3ème Colloque R&T Ecoulements Internes en Propulsion Solide*, ONERA, Châtillon, Vol. 3, 1998, pp. 1–32.

[29]Powell, A., "Theory of Vortex Sound," *Journal of Acoustical Society of America*, Vol. 36, No. 1, 1964, pp. 177–195.

[30]Howe, M. S., "Contributions to the Theory of Aerodynamic Sound, with Application to Excess Jet Noise and the Theory of the Flute," *Journal of Fluid Mechanics*, Vol. 71, 1975, pp. 625–673.

[31]Anthoine, J., and Olivari, D., "Cold Flow Simulation of Vortex-induced Oscillations in a Model of Solid Propellant Boosters," AIAA Paper 99-1826, May 1999.

[32]Anthoine, J., and Buchlin, J.-M., "Nozzle Design Effect on Vortex Induced Instabilities in an Axial Injected Cold Flow Model of the Ariane-5 EAP," *Proceedings of the Inter-Noise 2000*, Sfa and INRETS, Paris, 2000.

[33]Godfroy, F., Jacquemin, P., Tissier, P. Y., and Jouve, F., "Three Dimensional Simulation of Unsteady Inviscid Flows Using a Second Order Finite Volume Method. Application to Flows Inside Solid Propellant Motors," *Computing Methods in Applied Sciences and Engineering*, edited by Glowinski, Nova Science Publishers, Incorporated, New York, 1992.

[34]Durand, P., Vieille, B., Lambaré, H., Vuillermoz, P., Bouré, G., Steinfeld, P., Godfroy, F., Guéry, J. F., "CPS: A Three-Dimensional CFD Numerical Code Dedicated to Space Propulsive Flows," AIAA Paper 2000-3864, 2000.

[35]Comte, P., and Lesieur, M., "Large-Eddy Simulations of Compressible Turbulent Flows," *Advances in Turbulence Modelling*, Vol. 1998-05, von Karman Inst., Rhode Saint Genèse, 1998.

[36]Anthoine, J., "Experimental and Numerical Study of Aeroacoustic Phenomena in Large Solid Propellant Boosters," Ph.D. Dissertation, Univ. Libre de Bruxelles, Brussels, Oct. 2000.

[37]Anthoine, J., Planquart, P., and Olivari, D., "Cold Flow Investigation of the Flow Acoustic Coupling in Solid Propellant Boosters," AIAA Paper 98-0475, Jan. 1998.